Magnetoresistance and Microstructure of Magnetite Nanocrystals Dispersed in Indium−Tin Oxide Thin Films

Koichi Okada,[†] Shigemi Kohiki,*,[†] Masanori Mitome,[†] Hidekazu Tanaka,[§] Masao Arai,[†] Masaki Mito,[||] and Hiroyuki Deguchi[||]

Departments of Materials Science and of Basic Science, Kyushu Institute of Technology, 1-1 Sensui, Tobata, Kitakyushu 804-8550, Japan, National Institute for Materials Science, 1-1 Namiki, Tsukuba, Ibaraki 305-0044, Japan, and Institute of Scientific and Industrial Research, Osaka University, 8-1 Mihogaoka, Ibaraki, Osaka 567-0047, Japan

ABSTRACT Epitaxial indium−tin oxide (ITO) thin films were fabricated on a yttria-stabilized zirconia (YSZ) substrate by pulsed-laser deposition using magnetite (Fe_3O_4) nanoparticle dispersed ITO powders as a target. Magnetoresistance of the film at a field of 1 T was 39 % at 45 K, and it stayed at 3 % above 225 K. The film demonstrated cooling hysteresis in the temperature dependence of direct-current magnetization. Transmission electron microscopy revealed that phase-separated Fe_3O_4 nanocrystals with widths of $\approx 40-150$ nm and heights of $\approx 10-25$ nm precipitated and grew epitaxially on the substrate in the film. Both the $Fe_3O_4(111)$ and ITO(001) planes were parallel to the YSZ(001) plane. The $Fe_3O_4(11-2)$ and -(1−10) planes were parallel to the ITO(100) and -(010) planes, respectively, and the planes connected smoothly at the grain boundary. The contour map of the electron density for the $Fe_3O_4(111)$ plane by the first-principles electronic structure computation was similar to that for the ITO(001) plane. The [111]-oriented Fe_3O_4 nanocrystals played the role of spin aligner for charge carriers of the epitaxial ITO film.

KEYWORDS: magnetoresistance • microstructure • magnetite nanocrystals • indium−tin oxide thin film • epitaxial growth • pulsed-laser deposition

INTRODUCTION

Intense research has been carried out on room temperature ferromagnetism (RT-FM) of transparent conducting oxides (TCOs) doped with 3d transition-metal elements to explore promising material realizing transparent spintronics devices (1−20). Substitution of cation sites by the doped atoms was believed to be indispensable for realizing RT-FM in TCOs, while RT-FM in TCOs caused by ferromagnetic metal clusters of the doped elements has also been reported (2, 4, 19). Indium−tin oxide (ITO) is the most widely used TCO in the semiconductor and electronic device industries. RT-FM was manifested for ITO films doped with Mn (8), Cr (13), and Fe (18). Pulsed-laser-deposited (PLD) thin films grown heteroepitaxially on a yttria-stabilized zirconia (YSZ) substrate in oxygen partial pressures of $10^{-3}-10^{-1}$ Pa exhibited RT-FM due to nanocrystals (NCs) of γ-Fe_2O_3 dispersed in ITO (18). The mismatch between the lattice constant of the a axis of In_2O_3 (1.0118 nm) and twice that of YSZ (0.5139 nm) amounted to 1.6 %. RT-FM due to phase-separated Fe_3O_4 nanoparticles dispersed in ITO was also reported for the powders heat-treated at 900 °C in flowing argon gas (20). It is well-known that Fe_3O_4 has the fully spin-polarized half-metallic band structure with a Curie temperature of 858 K, and it is highly conducting at room temperature. ITO-containing phase-separated Fe_3O_4 NCs are anticipated to exhibit RT-FM due to charge carriers with spins parallel to the minority spins of Fe_3O_4 when the $Fe_3O_4[111]$ axes of the NCs are parallel with each other.

Here, we report magnetoresistance (MR) and transmission electron microscopy (TEM) of epitaxial ITO films fabricated on a YSZ substrate by using the Fe_3O_4 nanoparticle dispersed ITO powders as a PLD target in oxygen partial pressures lower than 5×10^{-6} Pa. The ratio of electrical resistance measured with a field of $H = 1$ T to that measured without a field varied from 0.72 at 45 K to 0.97 above 225 K with rising temperature. TEM revealed that phase-separated Fe_3O_4 NCs with widths of $\approx 40-150$ nm and heights of $\approx 10-25$ nm precipitated and grew epitaxially on the substrate in the film. The $Fe_3O_4[111]$ axis of each NC was vertical to the film surface. A smooth connection in the electron density distribution between the $Fe_3O_4(111)$ and ITO(001) planes was simulated by the first-principles electronic structure computation.

EXPERIMENT AND COMPUTATION

Pulsed-Laser Deposition. We synthesized the Fe_3O_4 nanoparticle dispersed ITO powders for preparation of the PLD target. For the synthesis of ITO powders, weighed powders of In_2O_3 and SnO_2 with a molar ratio of In:Sn = 1.95:0.05 were mixed by grinding, and then heated at 1200 °C in flowing argon gas. The ITO powders were soaked in an ethanol solution of $FeCl_3$ and then dried and heated at 900 °C in flowing argon gas.

The molar ratio of In:Fe = 2:0.15 was determined by energy-dispersive X-ray analysis. The Fe_3O_4 nanoparticle dispersed ITO powders demonstrated X-ray diffraction (XRD) peaks attributable to the C-rare-earth-type In_2O_3 cubic cell. No XRD peak from any iron-related compounds appeared, while the temperature dependence of direct-current magnetization ($M-T$ curve) showed cooling hysteresis and a cusp around 120 K (see Figure S1 in the Supporting Information), which corresponds to the Verwey transition temperature (T_V) of Fe_3O_4 bulk (20). For usage as a target of pulsed-laser deposition, the Fe_3O_4 nanoparticle dispersed ITO powders were pelletized and then sintered at 1500 °C for 1 h in flowing oxygen gas. Thin films were grown on the (001) surface of a YSZ substrate at 600 °C in a pressure lower than 5×10^{-6} Pa by using the Fe_3O_4 nanoparticle dispersed ITO target. An ArF excimer laser with a wavelength of 193 nm was focused onto the target. The repetition rate and energy density were 3 Hz and 1 J/cm^2, respectively. The deposition rate was ≈0.01 nm/s. XRD patterns of the films were measured with a Rigaku CN2013 diffractometer using Cu Kα radiation.

Physical Properties, Microstructure, and Chemical States. For electric and magnetic measurements, we used a Quantum Design superconducting quantum interference devise (SQUID) magnetometer (MPMS 5S). Platinum electrodes with thicknesses of a few 100 nm were made by sputtering on the films, and they were bonded by gold wires to the system. For $M-T$ measurement, the sample was cooled from room temperature to 5 K in zero field, and then a field of $H = 100$ Oe was applied. We measured zero-field-cooled (ZFC) magnetization with rising temperature up to 300 K. After the measurement, the sample was cooled again to 5 K in the same field, and then field-cooled (FC) magnetization was measured with increasing temperature to 300 K. Diamagnetism of both the ITO film and the YSZ substrate were compensated for by using a bit of lead metal. The microstructure of the films was examined by a JEOL JEM-3100FEF transmission electron microscope operated at an electron acceleration voltage of 300 kV. The transmission electron microscope has an in-column Ω-type energy filter that is useful in removing the inelastic scattering contribution from electron diffraction patterns and mapping elemental distributions from energy-filtered images with ~0.5 nm spatial resolution. The iron maps representing distribution of iron atoms were obtained from the Fe L_3 electron energy loss signal. An energy-dispersive X-ray spectrometer attached on the transmission electron microscope was also used for elemental analysis. X-ray absorption near-edge structure (XANES) measurement was carried out at the BL15 in the SAGA Light Source, Japan. The Fe K-edge spectrum was collected at room temperature with an energy resolution of $10^{-4}-10^{-3}$ by the conversion electron yield method.

Computation. The first-principles computation was carried out to examine in detail the connection in the electron density between the $Fe_3O_4(111)$ and $In_2O_3(002)$ planes. The calculations were performed using the WIEN2k code, which is based on the APW + lo method (21). We used the generalized-gradient approximation for density functional theory. Muffin-tin radii were chosen as 1.93 au for indium, 1.83 au for iron, and 1.62 au for oxygen. The cutoff wavenumber K for basis functions was set as $Rk = 6.0$, where R is the smallest muffin-tin radius of 1.62 au. The number of k points in an irreducible Brillion zone was chosen as 100. With these parameters, sufficient numerical convergences were achieved.

RESULTS AND DISCUSSION

Epitaxial Growth and MR of the ITO Film. As shown by the inset of Figure 1, upper panel, the XRD pattern indicates that the ITO film grew epitaxially on the YSZ substrate. We observed intense (h00) reflections from a In_2O_3 cubic cell along with those of a YSZ cubic cell.
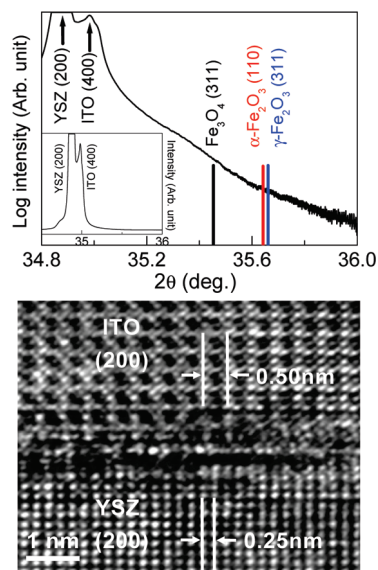
FIGURE 1. XRD pattern in the vicinity of the YSZ(200) and ITO(400) reflections (upper panel). The peaks from magnetite(311), hematite(110), and maghemite(311) planes appear at $2\theta = 35.453°$ (JCPDS 19-0629), 35.642° (JCPDS 33-0664), and 35.661° (JCPDS 39-1346), respectively, in XRD with Cu Kα X-rays. The intensity of the figure is logarithmic, and that of the inset is normal. HRTEM image around the interface between the film and substrate (lower panel).

Furthermore, no peak from the iron-related phase appeared, as is seen in the upper panel of Figure 1. The lattice constant a of the ITO film estimated from the (006) reflection was 1.008 nm. It is well-known that the ionic radius of the Sn^{4+} ion is smaller than that of the In^{3+} ion. The a value of the C-rare-earth-type cubic cell was decreased by Sn^{4+} ion substitution for the In^{3+} ion. The mismatch between the lattice constant of the a axis of the ITO film and twice that of the YSZ substrate amounted to 1.9%. As shown in the lower panel of Figure 1, the high-resolution TEM (HRTEM) image reconfirmed epitaxial growth of the ITO film on the YSZ substrate. Parallelism between the ITO(002) and YSZ(002) planes seen in the HRTEM image is consistent with that observed by XRD. The ITO(200) plane is parallel to the YSZ(200) plane. The epitaxial orientation relationship between the film and substrate can be expressed as ITO(001)∥YSZ(001) and ITO[100]∥YSZ[100].

Figure 2 shows the temperature dependence of resistance measured with (R_H) and without (R_0) the magnetic field. Both resistance curves showed smooth decreases with rising temperatures. No sudden change at T_V is similar to that reported for the [111]-oriented Fe_3O_4 film (22). As shown by the inset of Figure 2, the R_H/R_0 value increased from 0.72 to 0.97 with a rise of the temperature from 45 to 225 K, and the value remained constant above 225 K. The values at 75 and 165 K were 0.74 and 0.95, respectively. R_H/R_0 above 225 K is almost the same as that reported as 0.98 at 300 K for the Fe_3O_4 films (22). MR defined as $100(R_0 - R_H)/R_H$ at 45, 75, 105, 165, and above 225 K amounted to 39, 35, 18, 5, and 3%, respectively. We observed a significant rise in MR with decreasing temperature below 165 K, which is similar to that reported (22) below ≈180 K. The ratio of MR at 75 K to that at 165 K for the film (≈7) was rather larger than the one (≈3.3) reported (22). Such a change in MR is
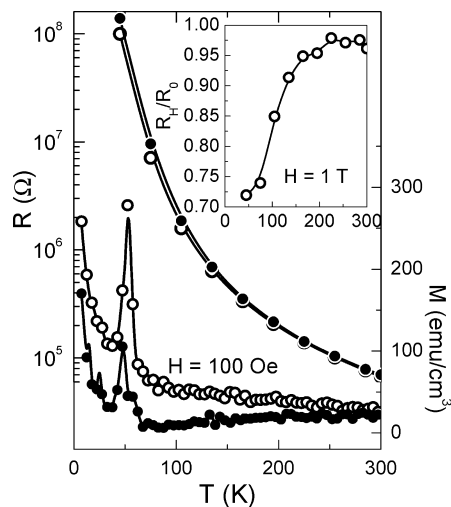
FIGURE 2. R_H (open circles) and R_0 (closed circles) of the film (left scale) with $H = 1$ T applied in the film plane. FC (open circles) and ZFC (filled circles) $M-T$ data at $H = 100$ Oe (right scale). Inset: temperature dependence of R_H/R_0.
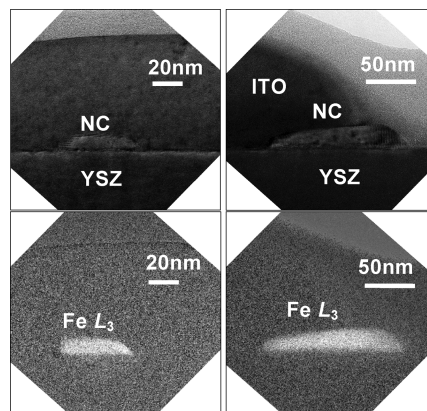

FIGURE 3. TEM images (upper panels) and iron maps (lower panels) for a smaller NC (left) and a larger NC (right). The iron maps obtained from the Fe L_3 electron energy loss signal represent distribution of the iron atoms in the film.

intriguing in relation to the film structure with the Fe_3O_4 and ITO heterointerface or with the Fe_3O_4 antiphase grain boundary (22). As mentioned below, the sample includes Fe_3O_4 NCs with the [111] axis vertical to the film plane. Because the [111] axis is the easy magnetization axis of the cubic Fe_3O_4 crystal, the magnetocrystalline anisotropy of the Fe_3O_4 crystal brings about the spontaneous magnetization vertical to the film plane. The magnetizations oriented upward and downward are possible and equivalent for each NC without an external magnetic field. When we assume that magnetic coupling over a large fraction of the NCs is antiferromagnetic, there is a high resistance for the spin-polarized electrons between the adjacent NCs. By application of the magnetic field, the antiferromagnetically coupled spins are forced to align along the external field, and then transfer of the spin-polarized electrons will be enhanced.

MR of the film varied rapidly from 75 to 165 K; however, we found no magnetic anomaly at the temperatures in the $M-T$ curves, as shown in Figure 2. The film exhibited divergence between FC and ZFC magnetization. Above 50 K, the $M-T$ curves of the film correspond well to that reported for the Fe_3O_4 nanoparticles with diameters of 50 nm (23). A broad maximum centered around 300 K in the ZFC magnetization, corresponding to blocking of superparamagnetic moments, was also reported for the Fe_3O_4 nanoparticles with diameters of 50 nm (23). It is known for Fe_3O_4 that shrinkage in the nanoparticle diameter and in the film thickness lowers T_V (24). Such magnetic behavior suggests that the ITO film is a magnetically diluted system of phase-separated Fe_3O_4 NCs (25), while MR of the ITO film indicates that the carriers are highly spin-polarized, almost the same as the epitaxial Fe_3O_4 films (26).

Precipitation and Epitaxy of Fe_3O_4 NCs. By using TEM, we observed phase-separated Fe_3O_4 NCs with widths of ≈40−150 nm and heights of ≈10−25 nm located at the interface between the ITO film and the YSZ substrate. As shown in the upper left panel of Figure 3, the surface of the ITO film with a thickness of ≈75 nm is smooth, and a NC

with a width and height of ≈40 and ≈10 nm, respectively, is located at the film−substrate interface. The NC includes iron atoms, as shown by the lower left panel of Figure 3. The width and height of the NC including iron atoms reached ≈150 and ≈25 nm, respectively, for a larger NC, as shown in the upper and lower right panels of Figure 3. Interestingly, both the smaller and larger NCs positioned at the film−substrate interface. Precipitation of metal clusters of the doped elements in oxide has been reported rather frequently, such as metallic cobalt clusters in TiO_2 thin films (19), though there has been no report on NCs of metal oxides epitaxially grown on a substrate in TCO films.

NCs of inverse-spinel-type Fe_3O_4 grew epitaxially on the YSZ substrate, as shown in Figure 4. Two kinds of orientations were observed for Fe_3O_4 NCs from electron diffraction analysis. One is a [1−10] incidence, and the other is a [11−2] incidence. In both orientations, the Fe_3O_4(111) plane is always parallel to the YSZ(002) plane. One orientation can be reproduced by rotating the other orientation by 90°. The YSZ(001) surface and ITO crystal have 4-fold symmetry along the surface normal, and thus the two orientations are equivalent to each other. The Fe_3O_4 NCs can be rotated along the surface normal by each 90°, and four types of orientations are possible.

A cubic structure for iron oxide that is different from the inverse-spinel-type Fe_3O_4 ($a = 0.8396$ nm) is well-known as γ-Fe_2O_3 ($a = 0.8346$ nm). Lattice constants for the structures are very close, and it is difficult to distinguish one from the other. However, the space groups are different for each other. It is $Fd\bar{3}m$ for Fe_3O_4 and $P4_132$ for γ-Fe_2O_3. {112} reflections are forbidden in $Fm3m$ symmetry, but they are allowed in $P4_332$ symmetry. The electron diffraction pattern demonstrated no {112} reflection marked as × in the middle left panel of Figure 4, and thus it is clear that the NCs are Fe_3O_4 crystals.

We reconfirmed that the chemical state of the NC including Fe atoms in the ITO film is Fe_3O_4 by the XANES spectrum shown in Figure 5. It is well-known that in the XANES spectra of 3d transition-metal oxides photoexcitation of a 1s electron into the 3d−4p mixed states at the central atom and the 4p continuum states brings about the pre-edge and main peaks,
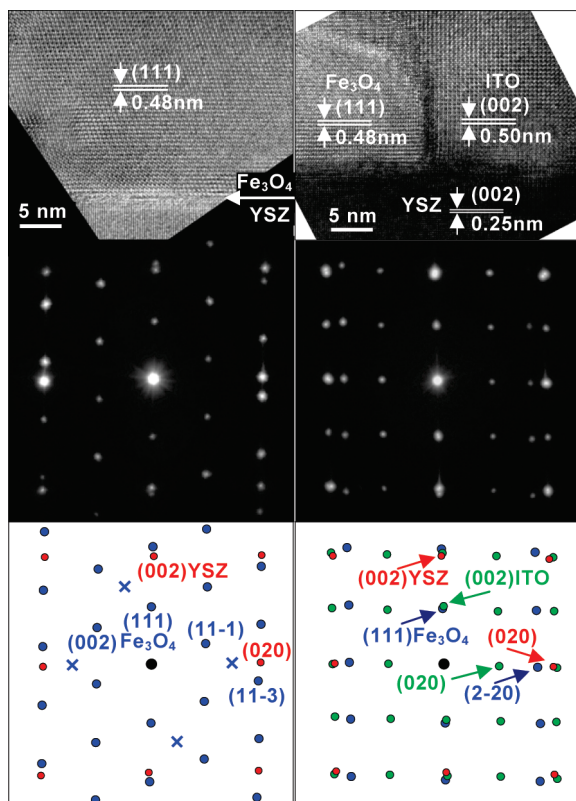
FIGURE 4. HRTEM image (upper panel), SAED pattern (middle panel), and indices corresponding to the SAED pattern (lower panel) for the NC epitaxially grown on the substrate (left) and those for the NC and the film epitaxially grown on the substrate (right). The electron beam incidence was $[1-10]$ on Fe_3O_4 and $[100]$ on YSZ (left), and it was $[11-2]$ on Fe_3O_4 and $[100]$ on both ITO and YSZ (right). The mark $\times$ in the lower left panel corresponds to $\{112\}$ reflections. Epitaxial relations are $Fe_3O_4(111)\|YSZ(001)$, $Fe_3O_4[110]\|YSZ[100]$, $Fe_3O_4[1-1-2]\|YSZ[010]$, $ITO(001)\|YSZ(001)$, $ITO[100]\|YSZ[100]$, and $ITO[010]\|YSZ[010]$.
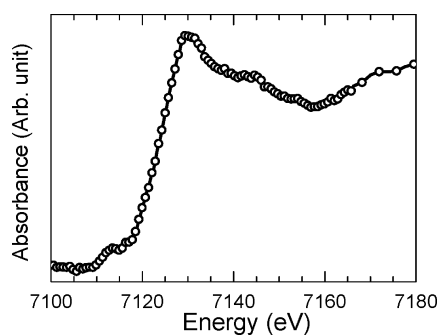

FIGURE 5. XANES spectrum at the Fe K edge of the film.

respectively. Furthermore, multiple scattering from neighboring atom shells forms the secondary peak appearing at >10 eV above the main peak. The pre-edge peak at 7113 eV, the main peak at 7130 eV, and the secondary peak at 7145 eV in Figure 5 agree well with those reported for Fe_3O_4 (27).

As it seen, the ITO film grew epitaxially even on the surface of the Fe_3O_4 NC. The most interesting fact is that iron atoms supplied from the PLD target were excluded and segregated from the single-crystalline ITO matrix and formed a truncated tetrahedron (Figure 6) of Fe_3O_4 on the substrate (28). In this figure, one example of the Fe_3O_4 orientations is shown. The Fe_3O_4 island can be rotated on the surface in
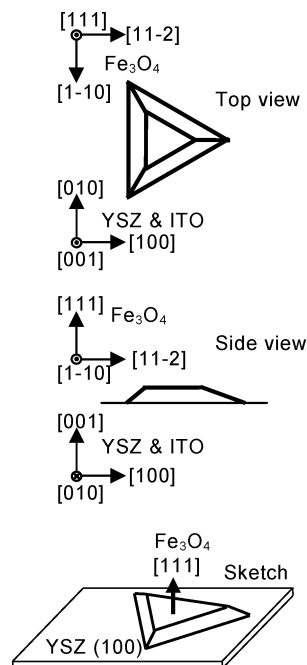

FIGURE 6. Illustration of the Fe_3O_4 NC on the YSZ substrate in the ITO film.

each 90° along the surface normal as mentioned before. Nucleation of three-dimensional islands is popular at the initial stage of thin film growth on a substrate having a different lattice constant. For release of the strain energy due to lattice mismatch, the three-dimensional island formation is effective even for films too thin to form dislocations (29). The mismatch between the lattice constant a of Fe_3O_4 and that of ITO is 16.7%. The mismatch between the lattice constant a of Fe_3O_4 and twice that of YSZ is 18.3%. The mismatch between Fe_3O_4 and YSZ or ITO (17−18%) is greatly larger than that between ITO and YSZ (1.9%). In pulsed-laser deposition, ITO formed a single-crystalline thin film, but Fe_3O_4 segregated to and formed the faceted islands on the substrate. The island looks like it has a fixed shape as it grows, as shown in Figure 3. From both electron energy loss spectroscopy and energy-dispersive X-ray spectroscopy in TEM, we obtained no evidence for the coexistence of iron in the ITO matrix and that of indium in the Fe_3O_4 NCs.

Spin-Polarized Carriers and the Fe_3O_4 NCs with the [111] Axis Vertical to the Film Surface. The Fe_3O_4 NC, precipitated and grown epitaxially on the substrate, formed a small-angle grain boundary to the epitaxially grown ITO matrix (the upper right panel of Figure 4). The first-principles computation was carried out to examine in detail the connection in the electron density between the $Fe_3O_4(111)$ and $In_2O_3(002)$ planes. As shown in Figure 7, the contour maps of the total electron density demonstrated a smooth connection between the $Fe_3O_4(111)$ and $In_2O_3(002)$ planes. The connection between the $Fe_3O_4(111)$ and the ITO(002) planes via a small-angle grain boundary is anticipated to support carrier transport with lesser carrier scattering in the film.

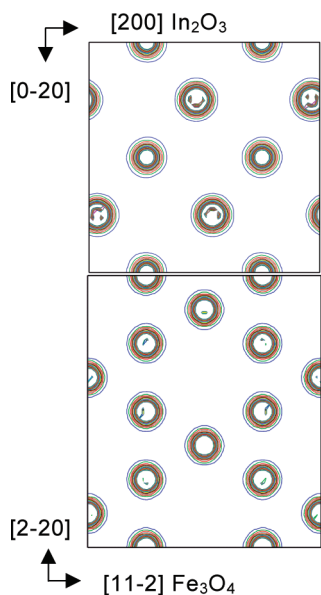The transport behavior in Fe_3O_4 bulk is known as a thermal activation type above T_V and a variable range

FIGURE 7. Contour maps of the total electron density of the $Fe_3O_4(111)$ and $In_2O_3(002)$ planes. The [11−2] and [220] axes of Fe_3O_4 are parallel to the [200] and [0−20] axes of In_2O_3, respectively.
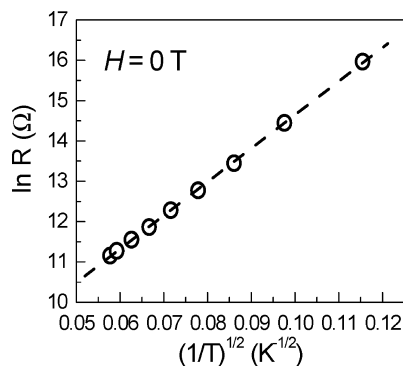

FIGURE 8. Temperature dependence of resistance of the film as a function of $(1/T)^{1/2}$.

hopping $R = R_0 \exp(a/T)^{1/4}$ type below T_V (22), while the ITO film, in which the Fe_3O_4 NCs exhibiting no anomaly at T_V are dispersed, demonstrated the transport character linearly fitted well with $(1/T)^{1/2}$. As shown by the $\ln R$ versus $(1/T)^{1/2}$ plots in Figure 8, carrier transport in the film above 45 K can be fitted well by the equation of $R \propto \exp(B/T)^{1/2}$, where $B = 4\alpha/k_B N(E_F)$. Here α is the coefficient of the exponential decay of the wavefunction, k_B is Boltzmann's constant, and $N(E_F)$ is the density of states at the Fermi level. Thus, $1/\alpha$ was found to be ≈ 3.2 nm. The temperature dependence of resistivity fitted well with $(1/T)^{1/2}$ was reported for sputter-deposited polycrystalline Fe_3O_4 films (30). The carrier transport of the film is controlled by the interface between the Fe_3O_4 NC and the ITO film and can be explained by a tunnelling conductance mechanism (31, 32). The observed linear relationship in the $\ln R$ versus $T^{-1/2}$ plot indicates that a distribution of energy barriers originated in the distribution of spacing between the NCs of the film. Spin-dependent tunnelling between ferromagnetic particles resulted in tunnelling MR of granular solids (33, 34), and tunneling MR is proportional to the spin polarization of the tunnelling elec-
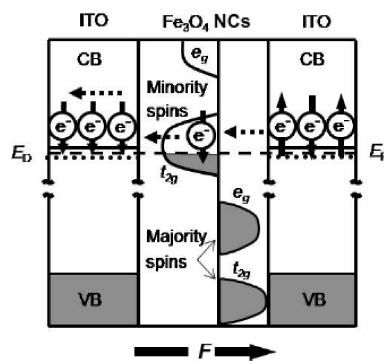

FIGURE 9. Schematic representation of the ITO film containing the [111]-oriented Fe_3O_4 NCs. Only the density of states of Fe^{2+} ions in octahedral sites was depicted for representing the half-metallicity of Fe_3O_4. Charge carriers of Fe_3O_4 are fully spin-polarized $(t_{2gi})^1$ at E_F. Even in a field F, only carriers of ITO with spins parallel to the minority spins of Fe_3O_4 pass through the NC. The Fe_3O_4 NCs play the role of a spin aligner for the carriers itinerating around the conduction band of the ITO film.

trons (35). Observed MR of the film is based on fully spin-polarized carriers transferred from Fe_3O_4 NCs.

For another cross-sectioned specimen of the films, we reconfirmed that the [111] axis of Fe_3O_4 for each NC was vertical to the film plane. Because the [111] axis is the easy magnetization axis of the cubic Fe_3O_4 crystal, the magnetocrystalline anisotropy of the Fe_3O_4 crystal brings about the spontaneous magnetization vertical to the film plane. Because of its half-metallic band structure, such Fe_3O_4 NCs can play the role of a spin aligner for the carriers of the epitaxial ITO film. As illustrated in Figure 9, fully spin-polarized carriers of Fe_3O_4 NCs transfer to the film and carriers of the film with spins parallel to the minority spins of Fe_3O_4 can pass through the NCs via E_F. Exchange interaction between carriers forces the rest of the carriers of ITO to align parallel to the minority spins of Fe_3O_4. A material such as the PLD film with fully spin-polarized carriers having T_c above room temperature is anticipated to fulfill the conditions indispensable for spintronics device applications.

CONCLUSIONS

We observed that epitaxial films fabricated in oxygen partial pressures lower than 5×10^{-6} Pa by using the Fe_3O_4 nanoparticle dispersed ITO powders as a PLD target exhibited MR almost the same as that of the epitaxial grown Fe_3O_4 films. MR at 45, 75, 105, 165, and above 225 K amounted to 39, 35, 18, 5, and 3%, respectively, in H of 1 T. R_H/R_0 increased from 0.72 to 0.97 with a rise of the temperature from 45 to 225 K. In TEM, we found segregation of the Fe_3O_4 NCs from the single-crystalline ITO film and formation of a truncated tetrahedron of Fe_3O_4 on the YSZ substrate. Phase-separated Fe_3O_4 NCs with widths of $\approx 40-150$ nm and heights of $\approx 10-25$ nm precipitated and grew epitaxially on the substrate in the film. Both the $Fe_3O_4(111)$ and ITO(001) planes were parallel to the YSZ(001) plane, and the $Fe_3O_4(111)$ and ITO(001) planes connected smoothly at a grain boundary. Such a smooth connection can be simulated by the first-principles computation of the electron density distribution and support the transport character linearly

fitted well with $(1/T)^{1/2}$ of the film. Because the $Fe_3O_4[111]$ axis for each NC was vertical to the film plane, the observed MR is based on fully spin-polarized carriers transferred from Fe_3O_4 NCs into the film. The [111]-oriented Fe_3O_4 NCs played the role of a spin aligner for the carriers of the epitaxial ITO film.

Supporting Information Available: SQUID data of the Fe_3O_4 nanoparticle dispersed ITO powders. This material is available free of charge via the Internet at http://pubs.acs.org.

REFERENCES AND NOTES

(1) Matsumoto, Y.; Murakami, M.; Shono, T.; Hasegawa, T.; Fukumura, T.; Kawasaki, M.; Ahmet, P.; Chikyow, T.; Koshihara, S.; Koinuma, H. *Science* **2001**, *291*, 854.

(2) Kim, D. H.; Yang, J. S.; Lee, K. W.; Bu, S. D.; Noh, T. W.; Oh, S. J.; Kim, Y. W.; Chung, J. S.; Tanaka, H.; Lee, H. Y.; Kawai, T. *Appl. Phys. Lett.* **2002**, *81*, 2421.

(3) Ueda, K.; Tabata, H.; Kawai, T. *Appl. Phys. Lett.* **2001**, *79*, 988.

(4) Kim, J. H.; Kim, H.; Ihm, Y. E.; Choo, W. K. *J. Appl. Phys.* **2002**, *92*, 6066.

(5) Sharma, P.; Gupta, A.; Rao, K. V.; Owens, F. J.; Sharma, R.; Ahuja, R.; Guillen, J. M. O.; Johansson, B.; Gehring, G. A. *Nat. Mater.* **2003**, *2*, 673.

(6) Ogale, S. B.; Choudhary, R. J.; Buban, J. P.; Lofland, S. E.; Shinde, S. R.; Kale, S. N.; Kulkarni, V. N.; Higgins, J.; Lanci, C.; Simpson, J. R.; Browning, N. D.; Das Sarma, S.; Drew, H. D.; Greene, R. L.; Venkatesan, T. *Phys. Rev. Lett.* **2003**, *91*, 077205.

(7) Coey, J. M. D.; Douvalis, A. P.; Fitzgerald, C. B.; Venkatesan, M. *Appl. Phys. Lett.* **2004**, *84*, 1332.

(8) Philip, J.; Theodoropoulou, N.; Berera, G.; Moodera, J. S.; Satpati, B. *Appl. Phys. Lett.* **2004**, *85*, 777.

(9) Hong, N. H.; Sakai, J.; Huong, N. T.; Poirot, N.; Ruyter, A. *Phys. Rev. B* **2005**, *72*, 045336.

(10) Yoo, Y. K.; Xue, Q.; Lee, H. C.; Cheng, S.; Xiang, X. D.; Dionne, G. F.; Xu, S.; He, J.; Chu, Y. S.; Preite, S. D.; Lofland, S. E.; Takeuchi, I. *Appl. Phys. Lett.* **2005**, *86*, 042506.

(11) He, J.; Xu, S.; Yoo, Y. K.; Xue, Q.; Lee, H. C.; Cheng, S.; Xiang, X. D.; Dionne, G. F.; Takeuchi, I. *Appl. Phys. Lett.* **2005**, *86*, 052503.

(12) Hong, N. H.; Sakai, J.; Huong, N. T.; Brize, V. *Appl. Phys. Lett.* **2005**, *87*, 102505.

(13) Kim, H. S.; Ji, S. H.; Kim, H.; Hong, S. K.; Kim, D.; Ihm, Y. E.; Choo, W. K. *Solid State Commun.* **2006**, *137*, 41.

(14) Philip, J.; Punnoose, A.; Kim, B. I.; Reddy, K. M.; Layne, S.; Holmes, J. O.; Satpati, B.; Leclair, P. R.; Santos, T. S.; Moodera, J. S. *Nat. Mater.* **2006**, *5*, 298.

(15) Hong, N. H.; Sakai, J.; Huong, N. T.; Brize, V. *J. Magn. Magn. Mater.* **2006**, *302*, 228.

(16) Peleckis, G.; Wang, X. L.; Dou, S. X. *Appl. Phys. Lett.* **2006**, *88*, 132507.

(17) Peleckis, G.; Wang, X. L.; Dou, S. X. *Appl. Phys. Lett.* **2006**, *89*, 022501.

(18) Ohno, T.; Kawahara, T.; Tanaka, H.; Kawai, T.; Oku, M.; Okada, K.; Kohiki, S. *Jpn. J. Appl. Phys.* **2006**, *45*, L957.

(19) Shinde, S. R.; Ogale, S. B.; Higgins, J. S.; Zheng, H.; Millis, A. J.; Kulkarni, V. N.; Ramesh, R.; Greene, R. L.; Venkatesan, T. *Phys. Rev. Lett.* **2004**, *92*, 166601.

(20) Okada, K.; Kohiki, S.; Nishi, S.; Shimooka, H.; Deguchi, H.; Mitome, M.; Bando, Y.; Shishido, T. *Jpn. J. Appl. Phys.* **2007**, *46*, L823.

(21) Blaha, P.; Schwartz, K.; Madsen, H. G. K.; Kvasnicka, D.; Luitz, J. *WIEN2k, An Augmented Plane Wave + Local Orbitals Program for Calculating Crystal Properties*; Techische Universitat Wien: Vienna, Austria, 2001.

(22) Ogale, S. B.; Ghosh, K.; Sharma, R. P.; Greene, R. L.; Ramesh, R.; Venkatesan, T. *Phys. Rev. B* **1998**, *57*, 7823.

(23) Goya, G. F.; Berquó, T. S.; Fonseca, F. C.; Morales, M. P. *J. Appl. Phys.* **2003**, *94*, 3520.

(24) Eerenstein, W.; Palstra, T. T. M.; Hibma, T.; Celotto, S. *Phys. Rev. B* **2002**, *66*, 20110(R).

(25) Sigmoidal behavior of magnetization M was observed in the field $H > \pm 2000$ Oe at 10 K. The order of M of the sample grown below the oxygen partial pressure of 5×10^{-6} Pa was 10^{-4} emu, which is larger by 2 orders of the magnitude than that for the films grown at the oxygen partial pressures of $1 \times 10^{-1} - 1 \times 10^{-3}$ Pa. Ohno, T.; Kawahara, T.; Murasugi, M.; Tanaka, H.; Kawai, T.; Kohiki, S. *J. Magn. Magn. Mater.* **2007**, *310*, e717.

(26) A change in the Hall resistance below the magnetic field of ± 1000 Oe amounted to 0.3 Ω/Oe, which is larger than that (0.02 Ω/Oe) in the field ranging from ± 1000 to $\pm 10\,000$ Oe. Because such changes are an indication of spin polarization of the film, X-ray magnetic circular dichroism measurement at the Fe $L_{2,3}$ edges using synchrotron radiation is indispensable for assertion.

(27) Subías, G.; García, J.; Blasco, J. *Phys. Rev. B* **2005**, *71*, 155103.

(28) The upper (111) plane of the Fe_3O_4 NC is widely spreading to and contacting ITO. If wider contact to ITO lowers the surface energy more for the NC, the NC surrounded by the (111) planes becomes more stable, and then the truncated octahedron is the most promising for the shape of the Fe_3O_4 NC.

(29) Tersoff, J.; LeGoues, F. K. *Phys. Rev. Lett.* **1994**, *72*, 3570.

(30) Liu, H.; Jiang, E. Y.; Bai, H. L.; Zheng, R. K.; Wei, H. L.; Zhang, X. X. *Appl. Phys. Lett.* **2003**, *83*, 3531.

(31) Sheng, P. *Phys. Rev. B* **1980**, *21*, 2180.

(32) Sheng, P. *Philos. Mag. B* **1992**, *65*, 357.

(33) Mitani, S.; Takahashi, S.; Takanashi, K.; Yakushiji, K.; Maekawa, S.; Fujimori, H. *Phys. Rev. Lett.* **1998**, *81*, 2799.

(34) Spin-dependent tunnelling between the Fe_3O_4 NCs is anticipated to cause significant tunnelling MR for the sample demonstrating semiconducting behavior. The first-principles computation on the $Fe_3O_4(110)/In_2O_3(010)$ interface was performed to obtain a better insight into the band structure in the vicinity of the atomically sharp Fe_3O_4 and ITO heterointerface. The interface was simulated by building up supercells consisting of $Fe_3O_4(110)$ layers on top of $In_2O_3(010)$ layers. The density of states of $Fe_3O_4(110)$ was metallic, and that of $In_2O_3(010)$ was semiconducting. At the In_2O_3 side, a large p-type density of states crossing E_F appeared in the layer positioned by 0.6 nm apart from the interface. Electrons doped to In_2O_3 occupy the empty states from 1 to 2 eV in the layer located next to the Fe_3O_4 surface. Therefore, nonmetallic carrier transport is rather reasonable in the vicinity of the Fe_3O_4 and ITO heterointerface. We will report on the computation in detail elsewhere.

(35) Inoue, J.; Maekawa, S. *Phys. Rev. B* **1996**, *53*, R11927.

AM9003057